


Cite this: *RSC Adv.*, 2025, 15, 2749

Improved self-powered perovskite $\text{CH}_3\text{NH}_3\text{PbI}_3/\text{SnO}_2$ heterojunction photodetectors achieved by interfacial engineering with a synergic effect

Guipeng Li,^a Huimin Zhang,^a Weihao Qin^b and Mingming Chen[✉]*^a

Lead halide perovskite heterojunctions have been considered as important building blocks for fabricating high-performance photodetectors (PDs). However, the interfacial defects induced non-radiative recombination and interfacial energy-level misalignment induced ineffective carrier transport severely limit the performance of photodetection of resulting devices. Herein, interfacial engineering with a spin-coating procedure has been studied to improve the photodetection performance of $\text{CH}_3\text{NH}_3\text{PbI}_3/\text{SnO}_2$ heterojunction PDs, which were fabricated by sputtering a SnO_2 thin film on ITO glass followed by spin-coating a $\text{CH}_3\text{NH}_3\text{PbI}_3$ thin film. It has shown that spin-coating of a SnO_2 layer on the sputtered SnO_2 thin films suppressed the surface oxygen vacancies of SnO_2 thin films and up-shifted their conduction band, which suppressed the interfacial non-radiative recombination and enhanced the carriers transport at the $\text{CH}_3\text{NH}_3\text{PbI}_3/\text{SnO}_2$ interface, respectively. Accordingly, improved photodetection performance, such as the reduced dark current and increased photocurrent, has been observed in the $\text{CH}_3\text{NH}_3\text{PbI}_3/\text{SnO}_2$ heterojunction PDs, where the responsivity and detectivity of 0.077 A W^{-1} and 2.0×10^{11} jones, respectively, at the zero bias have been demonstrated. These results show a simple way to suppress the interfacial non-radiative recombination and enhance the carrier transport at the interface to fabricate improved perovskite heterojunction PDs in the future.

Received 19th December 2024
Accepted 17th January 2025

DOI: 10.1039/d4ra08892a

rsc.li/rsc-advances

Introduction

Photodetectors (PDs), which convert photons into electric charge, have attracted much attention recently owing to their important applications in various areas including digital imaging, optical communications, medical analysis, and environment monitoring.^{1–4} In general, PDs can be classified into two categories, *i.e.*, photoconductors and photodiodes. The former ones possess a simple device structure but feature a high noise current and low photoconductive gains.⁵ In contrast, the latter ones have usually been characterized with a low noise current and high photon-to-electric conversion efficiencies owing to the presence of an interfacial barrier and a strong built-in electric field.^{6,7} Additionally, the photodiodes can operate without the requirement of a power supply. Heterojunctions, which are composed of two different semiconductors bound together, have been considered as important building blocks for photodiodes owing to simple fabrication process regarding free-of-controlled n- and p-type doping of selected semiconductors. In recent years, lead halide perovskites (LHPs) with a formula of ABX_3 (where A is the CH_3NH_3^+ (MA^+), and

$\text{HC}(\text{NH}_2)_2^+$ (FA^+); B is the Pb^{2+} ; X is the Cl^- , Br^- , and I^-) have attracted much attention from the optoelectronics community due to their outstanding properties such as long charge carriers lifetime, long charge carriers diffusion length, high absorption coefficient, widely tunable energy bandgap, and low-temperature solution processability.⁸ Benefiting from these advantages, LHP heterojunctions have been considered as promising candidates for achieving efficient photodetection.^{9–12}

Generally, the working principles of PDs are similar to those of solar cells (SCs), where excess carriers are generated due to the valance-band-to-conduction-band transition upon light illumination, followed by the collection of excess carriers by the electrodes. As a wide bandgap semiconductor, tin dioxide (SnO_2) features a high electron mobility, deep conduction band, and low-temperature processability, and has widely been employed as an electron transport layer to fabricate efficient SCs recently.^{13–15} Meanwhile, various PDs have recently been demonstrated based on LHP/ SnO_2 heterojunctions.^{16–18} Similar to LHP SCs, the performance of LHP PDs is mainly related to the collection efficiencies of excess carriers, which are limited by the trap-assisted non-radiative recombination and ineffective carrier transport.¹⁹ In heterojunction PDs, the former is mainly related to the bulk and interfacial defects, while the latter is owing to the energy-level misalignment at the heterojunction interface. Notably, various strategies have been explored to improve the crystalline quality of LHP thin films recently, which

^aDepartment of Microelectronics, Jiangsu University, Zhenjiang, Jiangsu 212013, China. E-mail: andychain@live.cn

^bSchool of Materials Science and Engineering, East China University of Science and Technology, Shanghai, 200237, China


facilitated the rapid development of power conversion efficiency (PCE) of LHP SCs.²⁰ Typically, doping of elements has resulted in an increase in grain sizes and a suppression of intrinsic defects (such as halide and Pb vacancies) in LHP thin films and nanocrystals.²¹ Besides, interfacial engineering with a thin dielectric layer and anchoring groups have been demonstrated but primarily to suppress the interfacial non-radiative recombination.²² In contrast, the alignment of energy-level at the heterojunction interface has seldom been explored before. Practically, both interfacial passivation and energy-level alignment are fundamental for fabricating high-performance heterojunction PDs.²³ Herein, we showed the fabrication of improved solution-processed MAPbI₃/SnO₂ heterojunction PDs by employing a stacked SnO₂ thin film prepared by sputtering and spin-coating methods in sequence. It showed that the subsequent spin-coating procedure behaved a synergic effect including a suppression of interfacial defects and alignment of the energy-level at the MAPbI₃/SnO₂ interface. Accordingly, a decreased dark current and an increased photocurrent have been demonstrated simultaneously in the MAPbI₃/SnO₂ heterojunction PDs. Finally, improved performance of photo-detection with the responsivity and detectivity as high as 0.077 A W⁻¹ and 2×10^{11} jones, respectively, at the zero bias have been evidenced.

Experiments

MAPbI₃/SnO₂ heterojunctions (Fig. 1b) were fabricated by spin-coating a MAPbI₃ thin film onto a stacked SnO₂ thin film, which was prepared by sputtering a SnO₂ thin film on cleaned ITO glasses then followed by spin-coating a thin SnO₂ layer. In detail, the ITO glasses were cleaned with acetone, ethanol and DI water in sequence. After that, a thin SnO₂ film was firstly grown using a sputtering method with a growth temperature of 500 °C and growth time of 10 min (labeled as SnO₂-1). The RF power is 80 W. The Sn source was provided by a SnO₂ target (99.99%). Ar/O₂ with a flow of 55 sccm/5 sccm were used as working gas. Then, a thin SnO₂ layer was grown by spin-coating to obtain the stacked SnO₂ thin films (labeled as SnO₂-2), in which the SnO₂ precursor solution (3 wt%) was prepared by diluting SnO₂ nanoparticles (~20 nm) into DI water. Finally, MAPbI₃ thin films were grown on SnO₂-2 (labeled as MAPbI₃-2) according to previous reports.²⁴ The perovskite precursor was prepared by dissolving PbI₂ and MAI into DMF/GBL/DMSO mixtures. The perovskite precursor was spin-coated with a two-step program (1000 rpm for 10 s and 5000 rpm for 20 s), where 400 μL toluene was dropped at 8 s of the second program. To reveal the roles of the spin-coated SnO₂ thin layer, MAPbI₃ thin films were directly prepared onto SnO₂-1 (labeled as MAPbI₃-1), as shown in Fig. 1a. The PDs were obtained by depositing a thin Au electrode with an area of 0.01 mm² on the MAPbI₃ thin films and an Ag paste on ITO.

The morphology and structure of SnO₂ and MAPbI₃ thin films were studied by field-emission scanning electron microscopy (SEM, JSM-7800F) and X-ray diffraction (XRD, Bruker D8 with Cu Kα radiation of 1.54 Å). The steady-state photoluminescence (PL) spectra of MAPbI₃ thin films were obtained

with the excitation of a cw 405 nm laser. The power of the incident laser was modulated by an attenuator. The transient PL spectra were excited with a ps-pulse laser at 450 nm, and the data were recorded by a ps time-correlated single photon counting technique. The absorption spectra were collected on an ultraviolet-visible spectrophotometer. The atomic electron binding energies of SnO₂ thin films were studied by X-ray photoelectron spectroscopy (XPS). The work function and energy band structure of SnO₂ were studied by ultraviolet photoelectron spectroscopy technique (UPS) using He I as the excitation source.

The performance of MAPbI₃/SnO₂ heterojunction PDs was studied by a photoresponse system consisting of a Xe lamp, a monochromator, an electronic shutter, two probes, a microscope, a Keithley 2401 source-measure unit (SMU), and a semiconductor parameter analyzer (Keysight, B1500A). All experiments were carried out in the atmosphere with a humidity of ~55–60%.

Results and discussions

Fig. 1c and d exhibit the SEM images of SnO₂-1 and SnO₂-2 thin films. It can be seen that the SnO₂-1 thin films feature a smooth surface (Fig. 1c). This can be attributed to the high growth temperature (500 °C, as mentioned above), which facilitated the migration of species at the substrate surface. In comparison, a rough surface has been observed in the SnO₂-2 thin films (Fig. 1d). According to previous report,²⁵ a rough surface of buried layer increases the contact area at the MAPbI₃/SnO₂ interface, which improves the optical absorption in the MAPbI₃ thin films. XRD were carried out to investigate the crystalline structures of SnO₂-1 and SnO₂-2 thin films, and the results are illustrated in Fig. 1i. As depicted, both the SnO₂ thin films exhibit a similar crystalline structure. According to the XRD peaks which are located at 22.3°, 33.5°, 36.8°, and 52.5°, both the SnO₂ thin films were crystallized into tetragonal with a space group of *P4₂/mnm*.

Fig. 1e and f exhibit the SEM images of MAPbI₃ thin films grown on SnO₂-1 and SnO₂-2. It shows that both the MAPbI₃ thin films have a dense structure, which is fundamental for the subsequent fabrication of heterojunction PDs. Notably, the grain sizes of MAPbI₃ thin films grown on SnO₂-2 are around 200 nm, which is slightly larger than those grown on SnO₂-1 (150 nm). In general, the MAPbI₃ thin films with a larger grain size possess a decreased density of boundary defects, which is favorable to improve the photodetection performance of resulting PDs.^{26,27}

Fig. 1j shows the XRD patterns of MAPbI₃ thin films grown on SnO₂-1 and SnO₂-2. It shows that both the MAPbI₃ thin films exhibit a similar crystalline structure and quality. Accordingly, the spin-coated SnO₂ layer did not affect the growth of MAPbI₃ thin films. Further observations show that the contact angle of SnO₂-2 is comparable to that of SnO₂-1 (Fig. 1g and h), which is responsible for the similar crystalline quality of the two MAPbI₃ thin films.

As mentioned above, the SnO₂-2 thin films were grown by sputtering and spin-coating SnO₂ layers in sequence. In the



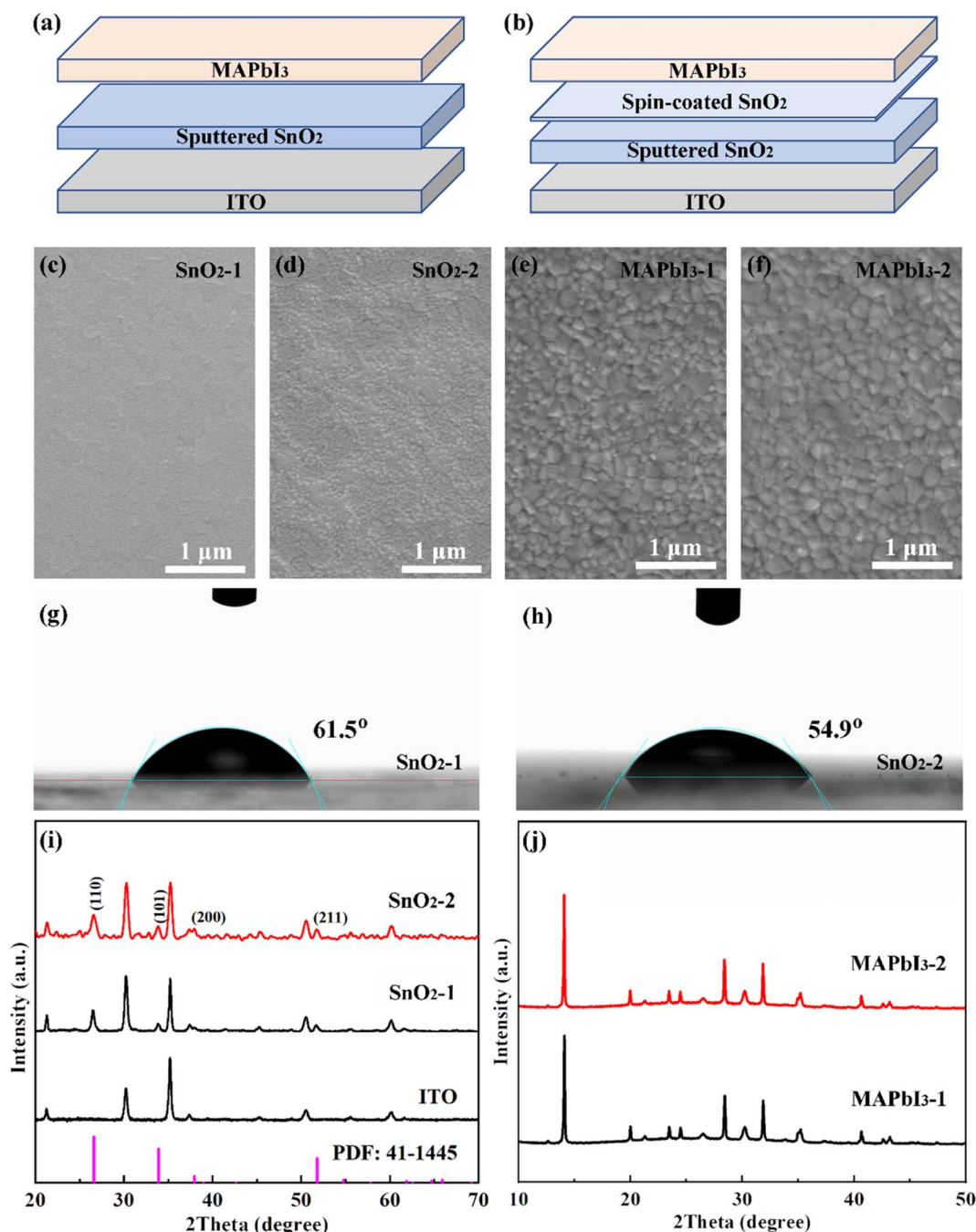


Fig. 1 Characteristics of SnO₂ and MAPbI₃ thin films. (a and b) Scheme of MAPbI₃/SnO₂-1 and MAPbI₃/SnO₂-2 heterojunctions. (c–f) SEM images of SnO₂ and MAPbI₃ thin films. (g and h) Water contact angles of SnO₂ thin films. (i and j) XRD patterns of SnO₂ and MAPbI₃ thin films.

latter case, the SnO₂ precursor was prepared by diluting the SnO₂ nanoparticles in DI water, therefore oxyhydroxyl groups (OH[−]) tended to be doped into the SnO₂ thin films.²⁸ To verify this, XPS measurements were performed, and the results are shown in Fig. 2. As depicted in Fig. 2a, only Sn and O signals were observed in both the SnO₂ thin films. This suggests that no impurities were incorporated during the preparation processes. Fig. 2b exhibits the O 1s core-level spectra of SnO₂-1 and SnO₂-2. The binding energies are observed at around 530.5 eV, 531.3 eV, and 532.5 eV, which are associated with Sn–O, oxygen vacancies

(V_O), and OH[−], respectively.²⁹ As reported, the content of various components can be qualitatively evaluated from their intensities of XPS peaks.²⁹ Accordingly, the SnO₂-2 shows an increased content of OH[−] and a reduced content of V_O compared to SnO₂-1. The former is related to the oxyhydroxyl groups in the aqueous solution. The reasons for latter are unclear currently, but should be related to the SnO₂ nanoparticles used. Importantly, it has reported that surface treatment with oxyhydroxyl groups tuned the energy band of buried layers.³⁰ As shown later, the SnO₂-2 thin films show an increased conduction band, which aligned the

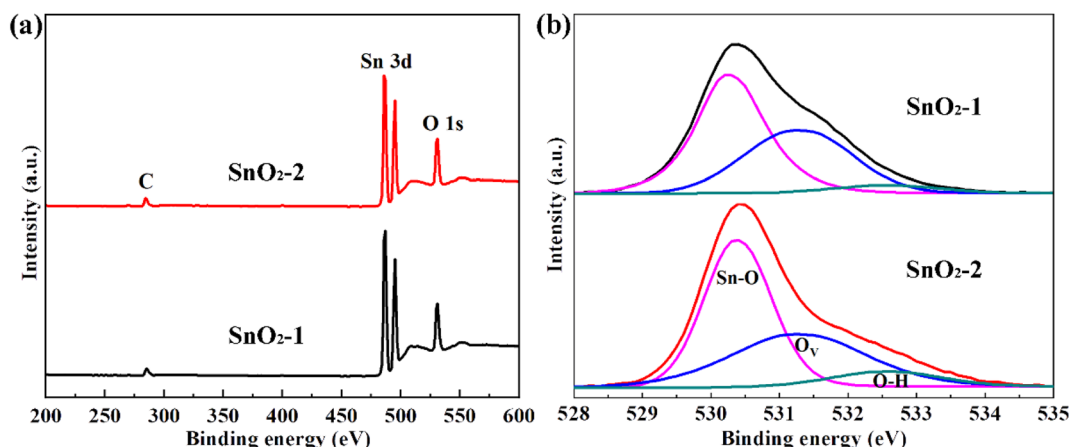


Fig. 2 XPS curves of SnO₂ thin films. (a) XPS survey spectra. (b) O 1s core-level spectra.

energy-level at the MAPbI₃/SnO₂ interface. Meanwhile, the reduced V_O suppressed the non-radiative recombination at the MAPbI₃/SnO₂ interface.³¹

Fig. 3 shows the steady-state and time-resolved PL spectra of MAPbI₃ thin films grown on SnO₂-1 and SnO₂-2. It can be seen that the PL spectra captured from the front surface of MAPbI₃ thin films exhibit similar intensity and lifetime (Fig. 3a and c), showing that both MAPbI₃ thin films possess similar crystalline quality. This is in consistence with the XRD and SEM results shown above. Notably, the PL spectra captured from the back surface of MAPbI₃ thin films exhibit distinct behaviors. As can be seen in Fig. 3b and d, the MAPbI₃ thin films prepared on SnO₂-2 exhibit a decreased PL intensity and lifetime. This suggests that the spin-coated SnO₂ layer enhanced the extraction of electrons at the MAPbI₃/SnO₂ interface. Similar phenomena have been reported in graphdiyne decorated MAPbI₃/SnO₂ and Mg²⁺ decorated MAPbI₃/NiO heterojunctions.^{32–34} As shown below, the slight up-shift of the conduction band of the SnO₂-2 thin films aligned the interfacial energy-level, which is responsible for the decreased PL intensity and lifetime in the back surface of MAPbI₃/SnO₂-2 heterojunctions.

Additionally, the interfacial defects at the MAPbI₃/SnO₂ interfaces were further studied from the excitation power dependent integrated PL, and the results are shown in Fig. 3e and f. As depicted in Fig. 3e, the PL spectra of both MAPbI₃ thin films exhibit similar patterns with an increase in excitation power, showing that the recombination processes of excess carriers kept unchanged. Fig. 3f depicts the relationship between integrated PL intensity and corresponding excitation power. According to the trap-filling model, the PL intensity increases slowly with an increase in excitation power under the low excitation level, while it increases rapidly with the excitation power under the high excitation level.^{17,35,36} As a result, the density of trap states (n_{trap}) is proportional to the excitation power threshold of complete trap filling (P_{th}), *i.e.*, $n_{\text{trap}} \propto P_{\text{th}}$.^{17,35,36} As shown in Fig. 3f, the P_{th} for MAPbI₃ grown on SnO₂-1 and SnO₂-2 were observed at 9.2 μW and 10.9 μW , respectively. This suggests that around 10% trap states have been reduced at the MAPbI₃/SnO₂-2 interface compared to MAPbI₃/SnO₂-1

interface. It is speculated that the reduced trap states at the MAPbI₃/SnO₂-2 interface is associated with the decreased surface V_O of the SnO₂-2 thin films as verified from XPS results shown above.

The energy band structure of SnO₂ thin films was further studied by UPS and UV-vis absorption results. Fig. 4 exhibits the UPS spectra of SnO₂-1 and SnO₂-2 thin films. As reported before, the valence band maximum (E_{V}) can be calculated from the following eqn (1):³⁷

$$E_{\text{V}} = -[h\nu - (E_{\text{cutoff}} - E_{\text{V}}^{\text{F}})] \quad (1)$$

where $h\nu$ is the photon energy of He I lamp (21.22 eV), E_{cutoff} is the cutoff energy of the secondary electrons, and E_{V}^{F} is the injection barrier (schematically shown in Fig. 4a). As shown in Fig. 4a and b, the E_{cutoff} are 16.31 eV and 16.20 eV, and the E_{V}^{F} are 3.41 eV and 3.17 eV for SnO₂-1 and SnO₂-2, respectively. This results in the E_{V} as -8.32 eV and -8.19 eV accordingly. In addition, according to the UV-vis absorption spectra shown in Fig. 4c and d, where the optical bandgap of SnO₂-1 and SnO₂-2 were obtained as around 4.1 eV, the corresponding conduction band minimums (E_{C}) were calculated as -4.19 eV and -4.02 eV. This demonstrates that the spin-coating procedure up-shifted the conduction band (+0.13 eV) of the SnO₂ thin films. Similar phenomena have been demonstrated in graphdiyne and NH₄S decorated SnO₂ thin films reported before.^{33,38,39} Accordingly, the energy band diagrams of SnO₂-1 and SnO₂-2 thin films were obtained, as shown in Fig. 4a and b inset.

After depositing thin circular Au electrodes on MAPbI₃ thin films and Ag paste on ITO, MAPbI₃/SnO₂ heterojunction PDs were fabricated. Fig. 5a illustrates the current-voltage (I - V) curves of MAPbI₃/SnO₂-1 and MAPbI₃/SnO₂-2 PDs captured in dark and under 540 nm illumination. As illustrated, the MAPbI₃/SnO₂-2 PDs shows a decreased dark current and an improved photocurrent compared to MAPbI₃/SnO₂-1 PDs. According to previous reports,^{17,40} the suppressed V_O at the surface of SnO₂-2 thin films is responsible for the reduced dark current and improved photocurrent. Besides, the up-shift of conduction band of SnO₂-2 thin films further increases the photocurrent.⁴¹ Fig. 5b shows the current-time curves of both



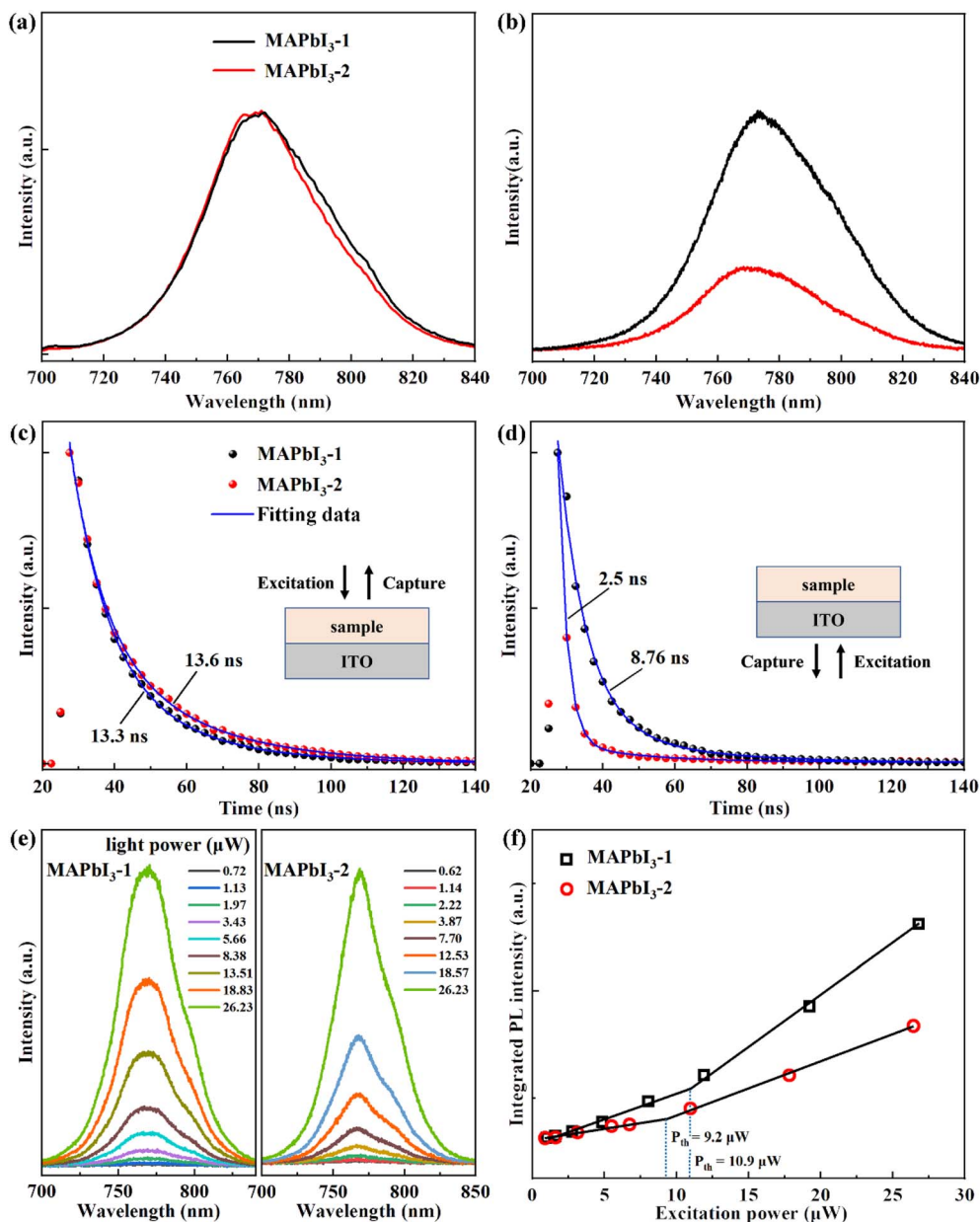


Fig. 3 Optical properties of MAPbI₃ thin films prepared on SnO₂-1 and SnO₂-2. (a and b) Steady-state and (c and d) transient PL spectra. (e and f) Excitation power dependent PL spectra. The PL data in a and c were captured from the front surface of MAPbI₃, as shown in Fig. 1c inset. The PL data in b, d, e and f were captured from the back surface of MAPbI₃, as shown in Fig. 1d inset.

PDs captured at zero bias with 540 nm illumination switched on and off. As shown, the photocurrent of both PDs increases linearly with an increase in light power, in which the slope of 0.06 A W⁻¹ and 0.02 A W⁻¹ for MAPbI₃/SnO₂-2 and MAPbI₃/SnO₂-1 PDs were derived (Fig. 5b inset). Generally, the increased slope of light power dependent photocurrent in MAPbI₃/SnO₂-2 PDs suggests the improved photodetection performance of them.

The photodetection performance of MAPbI₃/SnO₂ PDs was further evaluated from the responsivity and detectivity parameters. According to previous reports, the responsivity (R) and detectivity (D^*) were calculated using the following eqn (2) and (3):¹⁷

$$R = \frac{I_p - I_D}{P \times S} \quad (2)$$

$$D^* = \frac{R}{(2eI_D/S)^{0.5}} \quad (3)$$

where I_p and I_D are the photocurrent and dark current, S is the device area, P is the light power density (in W cm⁻²), and e is the electron charge. Fig. 5c and d exhibit the responsivity and detectivity of MAPbI₃/SnO₂-1 and MAPbI₃/SnO₂-2 PDs at zero bias. As shown, both the PDs shows a good photodetection performance in the UV to vis spectral range (350 nm–750 nm). Notably, the MAPbI₃/SnO₂-2 PDs exhibits an improved responsivity and detectivity (0.077 A W⁻¹ and 2×10^{11} jones), which



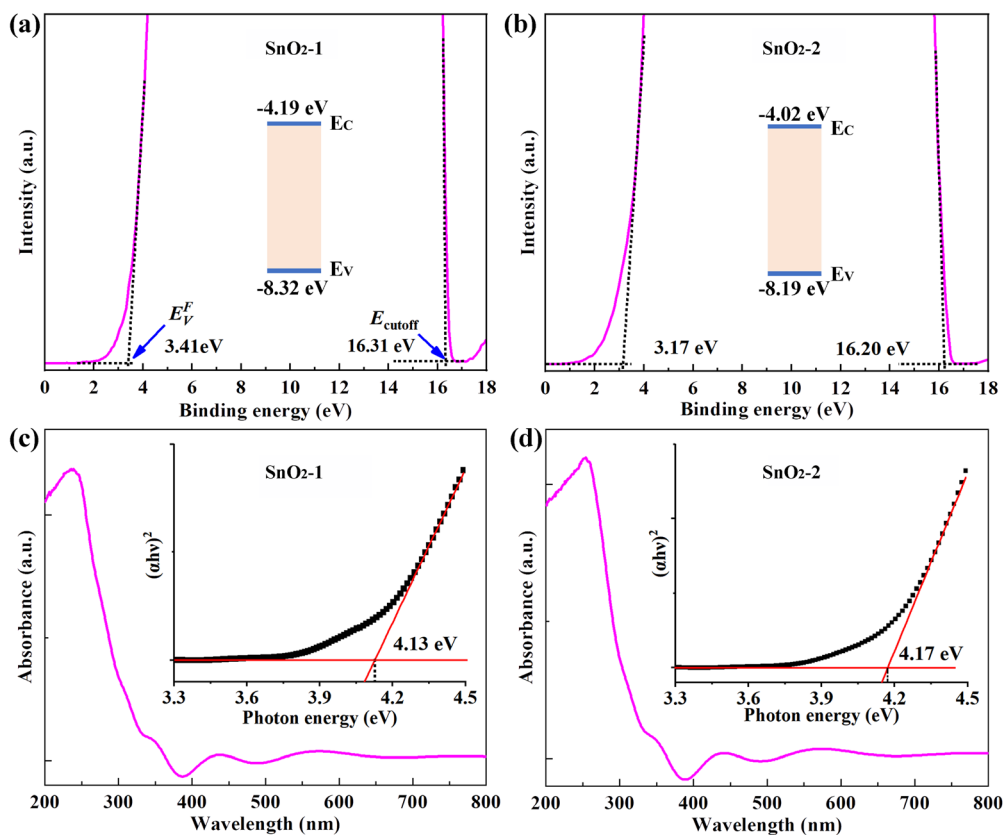


Fig. 4 (a and b) UPS and (c and d) absorption spectra of (a and c) SnO₂-1 and (b and d) SnO₂-2 thin films. The inset in (a and b) shows the energy band diagrams and in (c and d) shows the plot of $(\alpha h\nu)^2$ as a function of photon energy ($h\nu$).

are 2.5 times and 2 times higher than the MAPbI₃/SnO₂-1 PDs (0.03 A W⁻¹ and 1×10^{11} jones). As discussed above, the improved photodetection performance is attributed to the modification of the buried SnO₂ thin films in terms of reduced surface V_O and up-shift of conduction band. Meanwhile, a weak peak has appeared at around 850 nm in the responsivity and detectivity, which can be attributed to the defect-related absorption in the MAPbI₃ thin films.⁴²

Finally, the mechanisms of improved photodetection performance in MAPbI₃/SnO₂-2 PDs are discussed. Fig. 6 illustrates the photodetection processes of MAPbI₃/SnO₂-1 and MAPbI₃/SnO₂-2 PDs. Initially, electron-hole pairs were generated within the MAPbI₃ thin films upon illumination. Then, the electrons were extracted by the SnO₂ thin films owing to the interfacial electrical field and the holes moved toward the Au electrode. As a result, remarkable photocurrent has been observed in the MAPbI₃/SnO₂-1 and MAPbI₃/SnO₂-2 PDs. However, remarkable non-radiative recombination occurred at the MAPbI₃/SnO₂-1 interface (Fig. 6a) due to the high density of V_O at the surface of SnO₂-1 thin films. This resulted in an increased dark current and decreased photocurrent. In comparison, the non-radiative recombination was suppressed at the MAPbI₃/SnO₂-2 interface (Fig. 6b) owing to the suppressed V_O at the surface of SnO₂-2. Accordingly, improved photocurrent and decreased dark current have been observed

simultaneously in the MAPbI₃/SnO₂-2 PDs. Besides, the up-shift of conduction band of SnO₂-2 facilitated the electron transport at the MAPbI₃/SnO₂ interface (Fig. 6b), which further improved the photocurrent. Collectively, the spin-coating procedure behaved a synergic effect including reduced surface V_O and increased conduction band of the SnO₂, which accounted for the improved performance of photodetection of MAPbI₃/SnO₂-2 PDs.

In summary, performance-improved solution-processed MAPbI₃/SnO₂ heterojunction PDs have been fabricated by employing a stacked SnO₂ thin film prepared by sputtering and spin-coating methods in sequence. It has shown that the spin-coating procedure have little impacts on the growth of MAPbI₃ thin films, while it behaved a synergic effect such as reduced the surface V_O and up-shifted the conduction band of SnO₂ thin films. The former suppressed the interfacial non-radiative recombination, while the latter aligned the energy-level at the MAPbI₃/SnO₂ interface and further improved the carrier transport. On these basis, the MAPbI₃/SnO₂ heterojunction PDs with a stacked SnO₂ thin film exhibited an improved photodetection performance in terms of reduced dark current and increased photocurrent, where an improved responsivity and detectivity of 0.077 A W⁻¹ and 2.0×10^{11} jones, respectively, at the zero bias have been achieved. The results provided in this work provide a simple strategy for suppressing



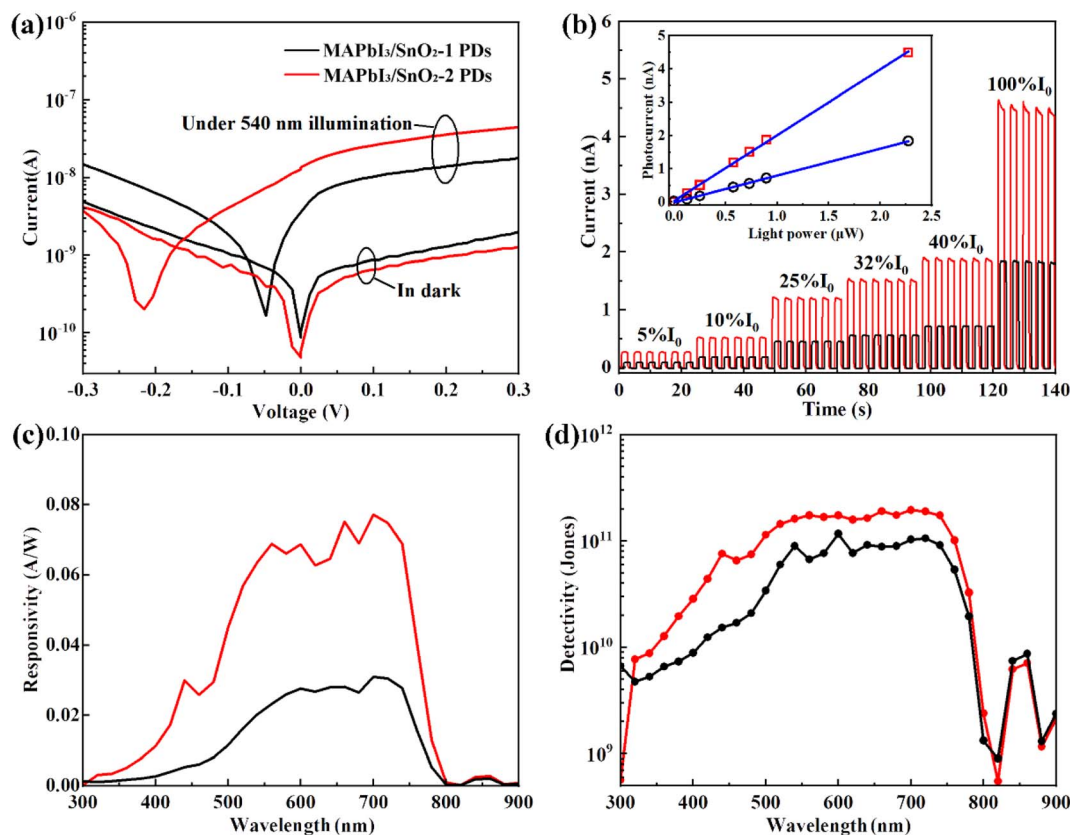


Fig. 5 Photodetection performance of MAPbI₃/SnO₂ PDs. (a) *I*-*V*. (b) Current-time curves. (c) Responsivity. (d) Detectivity. The bias in (b-d) is 0 V. The light was illuminated at the back surface of MAPbI₃ thin films.

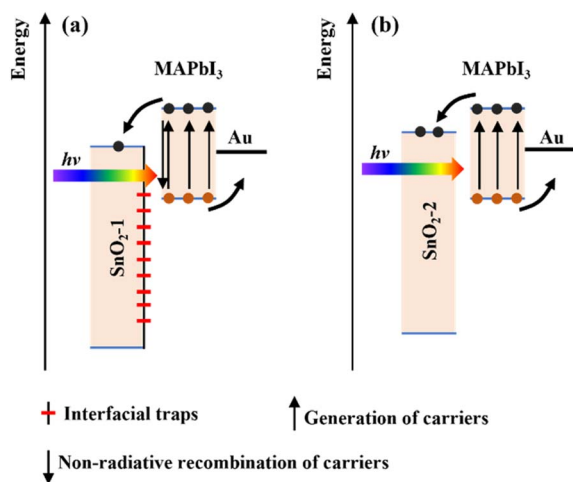


Fig. 6 Photodetection processes of (a) MAPbI₃/SnO₂-1 and (b) MAPbI₃/SnO₂-2 PDs.

the interfacial defects and aligning the energy-level simultaneously for improving the performance of perovskite heterojunction PDs in the future.

Data availability

The data that support the findings of this study are available from the corresponding authors upon reasonable request.

Conflicts of interest

The authors have declared that no conflict of interest exists.

References

- 1 L. Li, H. Chen, Z. Fang, X. Meng, C. Zuo, M. Lv, Y. Tian, Y. Fang, Z. Xiao, C. Shan, Z. Xiao, Z. Jin, G. Shen, L. Shen and L. Ding, An Electrically Modulated Single-Color/Dual-Color Imaging Photodetector, *Adv. Mater.*, 2020, **32**(24), 1907257.
- 2 W. Wu, X. Wang, X. Han, Z. Yang, G. Gao, Y. Zhang, J. Hu, Y. Tan, A. Pan and C. Pan, Flexible Photodetector Arrays Based on Patterned CH₃NH₃ PbI_(3-x)Cl_(x) Perovskite Film for Real-Time Photosensing and Imaging, *Adv. Mater.*, 2019, **31**(3), 1805913.
- 3 P. Büchele, M. Richter, S. F. Tedde, G. J. Matt, G. N. Ankah, R. Fischer, M. Biele, W. Metzger, S. Lilliu, O. Bikondoa, J. E. Macdonald, C. J. Brabec, T. Kraus, U. Lemmer and O. Schmidt, X-ray imaging with scintillator-sensitized hybrid organic photodetectors, *Nat. Photonics*, 2015, **9**(12), 843-848.
- 4 C. Bao, J. Yang, S. Bai, W. Xu, Z. Yan, Q. Xu, J. Liu, W. Zhang and F. Gao, High Performance and Stable All-Inorganic Metal Halide Perovskite-Based Photodetectors for Optical Communication Applications, *Adv. Mater.*, 2018, **30**(38), 1803422.



- 5 J. Liu, M. Gao, J. Kim, Z. Zhou, D. S. Chung, H. Yin and L. Ye, Challenges and recent advances in photodiodes-based organic photodetectors, *Mater. Today*, 2021, **51**, 475–503.
- 6 Y. Yan, Q. Wu, Y. Zhao, S. Chen, S. Hu, J. Zhu, J. Huang and Z. Liang, Air-Stable and Self-Driven Perovskite Photodiodes with High On/Off Ratio and Swift Photoresponse, *Small*, 2018, **14**(41), 1802764.
- 7 M. V. Kovalenko, L. Protesescu and M. I. Bodnarchuk, Properties and potential optoelectronic applications of lead halide perovskite nanocrystals, *Science*, 2017, **358**(6364), 745–750.
- 8 L. K. Ono, Y. Qi and S. Liu, Progress toward Stable Lead Halide Perovskite Solar Cells, *Joule*, 2018, **2**(10), 1961–1990.
- 9 D. Nodari, L. J. F. Hart, O. J. Sandberg, F. Furlan, E. Angela, J. Panidi, Z. Qiao, M. A. McLachlan, P. R. F. Barnes, J. R. Durrant, A. Ardanian and N. Gasparini, Dark Current in Broadband Perovskite-Organic Heterojunction Photodetectors Controlled by Interfacial Energy Band Offset, *Adv. Mater.*, 2024, **36**(33), 2401206.
- 10 Y. Zhang, C. Li, E. Bi, T. Wang, P. Zhang, X. Yang and H. Chen, Efficient Inverted Perovskite Solar Cells with a Low-Dimensional Halide/Perovskite Heterostructure, *Adv. Energy Mater.*, 2022, **12**(48), 2202191.
- 11 J. Zhuang, J. Wang and F. Yan, Review on Chemical Stability of Lead Halide Perovskite Solar Cells, *Nano-Micro Lett.*, 2023, **15**(1), 84.
- 12 J. Zhou and J. Huang, Photodetectors Based on Organic-Inorganic Hybrid Lead Halide Perovskites, *Adv. Sci.*, 2018, **5**(1), 1700256.
- 13 L. Xiong, Y. Guo, J. Wen, H. Liu, G. Yang, P. Qin and G. Fang, Review on the Application of SnO₂ in Perovskite Solar Cells, *Adv. Funct. Mater.*, 2018, **28**(35), 1802757.
- 14 Q. Jiang, X. Zhang and J. You, SnO₂: A Wonderful Electron Transport Layer for Perovskite Solar Cells, *Small*, 2018, 1801154.
- 15 C. Wu, B. Du, W. Luo, Y. Liu, T. Li, D. Wang, X. Guo, H. Ting, Z. Fang, S. Wang, Z. Chen, Y. Chen and L. Xiao, Highly Efficient and Stable Self-Powered Ultraviolet and Deep-Blue Photodetector Based on Cs₂AgBiBr₆/SnO₂ Heterojunction, *Adv. Opt. Mater.*, 2018, **6**(22), 1800811.
- 16 M. J. Paik, Y. Y. Kim, J. Kim, J. Park and S. I. Seok, Ultrafine SnO₂ colloids with enhanced interface quality for high-efficiency perovskite solar cells, *Joule*, 2024, **8**(7), 2073–2086.
- 17 P. Cheng, T. Zhao, M. Chen, S. Chen, X. Shen, Y. Liu, S. Yang, Z. Chen, X. Dong, Q. Wang and D. Cao, Improved Perovskite CH₃NH₃PbI₃ Thin Films by ZIF-67 Additive Assisted Co Ion Doping toward High-Performance and Stable Photodetectors, *Adv. Opt. Mater.*, 2023, **11**(21), 2300757.
- 18 Y. Lin, Y. Bai, Y. Fang, Z. Chen, S. Yang, X. Zheng, S. Tang, Y. Liu, J. Zhao and J. Huang, Enhanced Thermal Stability in Perovskite Solar Cells by Assembling 2D/3D Stacking Structures, *J. Phys. Chem. Lett.*, 2018, **9**(3), 654–658.
- 19 Z. Yang, Y. Deng, X. Zhang, S. Wang, H. Chen, S. Yang, J. Khurgin, N. X. Fang, X. Zhang and R. Ma, High-Performance Single-Crystalline Perovskite Thin-Film Photodetector, *Adv. Mater.*, 2018, **30**(8), 1704333.
- 20 D. Yang, R. Yang, K. Wang, C. Wu, X. Zhu, J. Feng, X. Ren, G. Fang, S. Priya and S. F. Liu, High efficiency planar-type perovskite solar cells with negligible hysteresis using EDTA-complexed SnO₂, *Nat. Commun.*, 2018, **9**(1), 3239.
- 21 T. Bu, J. Li, F. Zheng, W. Chen, X. Wen, Z. Ku, Y. Peng, J. Zhong, Y. B. Cheng and F. Huang, Universal passivation strategy to slot-die printed SnO₂ for hysteresis-free efficient flexible perovskite solar module, *Nat. Commun.*, 2018, **9**(1), 4609.
- 22 W. Jang, Z. U. Rehman, M. Haris, J. S. Cho, J. Lim, M. S. Kim, J.-C. Lee, H. K. Lee and D. H. Wang, Oxide vacancy passivation through interface engineering of Tetraphenylethylene-Based Small-Molecule with sulfonate functional group for efficient organic photodetector, *Chem. Eng. J.*, 2023, **472**, 144847.
- 23 M. Sun, H. Zhang, C. Liang, C. Ji, X. Jing, F. Sun, Q. Song, F. You and Z. He, Exploring Electron Transporting Layer in Combination with a Polyelectrolyte for n-i-p Perovskite Solar Cells, *Adv. Mater. Interfaces*, 2020, **7**(17), 2000412.
- 24 M. Abuhelaiqa, N. Shibayama, X.-X. Gao, H. Kanda and M. K. Nazeeruddin, SnO₂/TiO₂ Electron Transporting Bilayers: A Route to Light Stable Perovskite Solar Cells, *ACS Appl. Energy Mater.*, 2021, **4**(4), 3424–3430.
- 25 Y. Zheng, J. Kong, D. Huang, W. Shi, L. McMillon-Brown, H. E. Katz, J. Yu and A. D. Taylor, Spray coating of the PCBM electron transport layer significantly improves the efficiency of p-i-n planar perovskite solar cells, *Nanoscale*, 2018, **10**(24), 11342–11348.
- 26 W. Xu, G. Lei, C. Tao, J. Zhang, X. Liu, X. Xu, W. Y. Lai, F. Gao and W. Huang, Precisely Controlling the Grain Sizes with an Ammonium Hypophosphite Additive for High-Performance Perovskite Solar Cells, *Adv. Funct. Mater.*, 2018, **28**(33), 1802320.
- 27 B. Li, C. Liu and X. Zhang, SnO₂-Based Interfacial Engineering towards Improved Perovskite Solar Cells, *Nanomaterials*, 2024, **14**(17), 14171406.
- 28 J. Jia, C. Qian, Y. Dong, Y. F. Li, H. Wang, M. Ghoussoub, K. T. Butler, A. Walsh and G. A. Ozin, Heterogeneous catalytic hydrogenation of CO₂ by metal oxides: defect engineering – perfecting imperfection, *Chem. Soc. Rev.*, 2017, **46**(15), 4631–4644.
- 29 J. Liu, S. Li, S. Liu, Y. Chu, T. Ye, C. Qiu, Z. Qiu, X. Wang, Y. Wang, Y. Su, Y. Hu, Y. Rong, A. Mei and H. Han, Oxygen Vacancy Management for High-Temperature Mesoporous SnO₂ Electron Transport Layers in Printable Perovskite Solar Cells, *Angew. Chem., Int. Ed.*, 2022, **61**(26), 202202012.
- 30 X. Wang, Y. Zhang, C. Zhou, D. Huo, R. Zhang and L. Wang, Hydroxyl-regulated BiOI nanosheets with a highly positive valence band maximum for improved visible-light photocatalytic performance, *Appl. Catal., B*, 2020, **268**, 118390.
- 31 J. H. Lee, D. Shin, R. Rhee, S. Yun, K. M. Yeom, D. H. Chun, S. Lee, D. Kim, Y. Yi, J. H. Noh and J. H. Park, Band Alignment Engineering between Planar SnO₂ and Halide Perovskites via Two-Step Annealing, *J. Phys. Chem. Lett.*, 2019, **10**(21), 6545–6550.



- 32 H. Min, D. Y. Lee, J. Kim, G. Kim, K. S. Lee, J. Kim, M. J. Paik, Y. K. Kim, K. S. Kim, M. G. Kim, T. J. Shin and S. Il Seok, Perovskite solar cells with atomically coherent interlayers on SnO₂ electrodes, *Nature*, 2021, **598**(7881), 444–450.
- 33 S. Zhang, H. Si, W. Fan, M. Shi, M. Li, C. Xu, Z. Zhang, Q. Liao, A. Sattar, Z. Kang and Y. Zhang, Graphdiyne: Bridging SnO₂ and Perovskite in Planar Solar Cells, *Angew. Chem., Int. Ed.*, 2020, **59**(28), 11573–11582.
- 34 H. Park, R. Chaurasiya, B. H. Jeong, P. Sakthivel and H. J. Park, Nickel Oxide for Perovskite Photovoltaic Cells, *Adv. Photonics Res.*, 2021, **2**(8), 2000178.
- 35 Y. Zhu, Q. Cui, J. Chen, F. Chen, Z. Shi, X. Zhao and C. Xu, Inhomogeneous Trap-State-Mediated Ultrafast Photocarrier Dynamics in CsPbBr₃ Microplates, *ACS Appl. Mater. Interfaces*, 2021, **13**(5), 6820–6829.
- 36 X. Shen, S. Yang, M. Chen, J. Su, J. Cai, P. Cheng, Y. Liu, Q. Wang and D. Cao, Interfacial Engineering with Aluminum Oxide toward an Improved Self-Powered Narrowband Visible-Light Photodetection in Lead Halide Perovskite CH₃NH₃PbBr₃/p-Si Heterojunctions, *Adv. Mater. Interfaces*, 2022, **9**(14), 2102305.
- 37 N. Wu, T. Yang, Z. Wang, Y. Wu, Y. Wang, C. Ma, H. Li, Y. Du, D. Zhao, S. Wang, P. Liu, W. Huang, X. Ren, S. F. Liu and K. Zhao, Stabilizing Precursor Solution and Controlling Crystallization Kinetics Simultaneously for High-Performance Perovskite Solar Cells, *Adv. Mater.*, 2023, **35**(44), 2304809.
- 38 J. C. Schuurman, A. R. McNeill, R. F. Martinez-Gazoni, J. I. Scott, R. J. Reeves, M. W. Allen and A. J. Downard, The effect of covalently bonded aryl layers on the band bending and electron density of SnO₂ surfaces probed by synchrotron X-ray photoelectron spectroscopy, *Phys. Chem. Chem. Phys.*, 2019, **21**(32), 17913–17922.
- 39 Y. Ai, W. Liu, C. Shou, J. Yan, N. Li, Z. Yang, W. Song, B. Yan, J. Sheng and J. Ye, SnO₂ surface defects tuned by (NH₄)₂S for high-efficiency perovskite solar cells, *Sol. Energy*, 2019, **194**, 541–547.
- 40 L. Song, L. Huang, W. Xiao and J. Li, Improved performance and stability in CH₃NH₃PbI₃/Si heterojunction photodetectors realized by ZIF-67 additive assisted Co ion doping, *Appl. Phys. Lett.*, 2021, **118**(16), 033301.
- 41 E. H. Jung, B. Chen, K. Bertens, M. Vafaie, S. Teale, A. Proppe, Y. Hou, T. Zhu, C. Zheng and E. H. Sargent, Bifunctional Surface Engineering on SnO₂ Reduces Energy Loss in Perovskite Solar Cells, *ACS Energy Lett.*, 2020, **5**(9), 2796–2801.
- 42 J. Wang, X. Duan and W. J. Yin, Photoinduced Dynamic Defects Responsible for the Giant, Reversible, and Bidirectional Light-Soaking Effect in Perovskite Solar Cells, *J. Phys. Chem. Lett.*, 2021, **12**(38), 9328–9335.

